

Derivation of electric potential patterns in the inner magnetosphere from Cluster EDI data: Initial results

H. Matsui, V. K. Jordanova, J. M. Quinn, and R. B. Torbert

Space Science Center, University of New Hampshire, Durham, New Hampshire, USA

G. Paschmann

Max-Planck-Institut für Extraterrestrische Physik, Garching, Germany

Received 12 November 2003; revised 14 July 2004; accepted 5 August 2004; published 15 October 2004.

[1] Electric potential patterns are derived in the inner magnetosphere at $4 < L < 10$ using 2 years of data from the Electron Drift Instrument (EDI) on Cluster. First, we examine the relations between the electric field and the following three parameters to understand how the potential patterns are organized: B_Z component of the interplanetary magnetic field (IMF), Kp index, and Dst index. From these correlations we can determine the effect of the interplanetary electric field (IEF) on the inner magnetospheric electric field as measured by Cluster. Next, the electric field is related to a quantity proportional to the injection rate of the plasma sheet particles, $F(Dst^*) \equiv (dDst^*/dt + 0.13Dst^*)$, where the effect of the magnetopause current is removed in Dst^* . Then we develop a method to obtain potential patterns. An inverse problem is solved by adjusting a trade-off parameter for smoothness of the result. The obtained potential patterns for three controlling parameters, IMF B_Z , Kp index, and $F(Dst^*)$, are attached as supplemental material¹. We discuss the following features from these potential patterns: (1) potential drop, (2) rotation of the direction of the convection electric field, (3) dawn-dusk asymmetry of the strength of the electric field, and (4) size of the last closed equipotential (LCE). This initial study is relevant to the development of an empirical model of inner magnetospheric convection in the equatorial plane. *INDEX TERMS*: 2712 Magnetospheric Physics: Electric fields (2411); 2730 Magnetospheric Physics: Magnetosphere—inner; 2784 Magnetospheric Physics: Solar wind/magnetosphere interactions; 2794 Magnetospheric Physics: Instruments and techniques; *KEYWORDS*: electric potential patterns, inner magnetosphere, electron drift instrument

Citation: Matsui, H., V. K. Jordanova, J. M. Quinn, R. B. Torbert, and G. Paschmann (2004), Derivation of electric potential patterns in the inner magnetosphere from Cluster EDI data: Initial results, *J. Geophys. Res.*, *109*, A10202, doi:10.1029/2003JA010319.

1. Introduction

[2] Electric potential patterns have been investigated for a long time because the electric field is related to the transport of particles through $E \times B$ drifts. The electric field is a controlling parameter for the ring current evolution and decay as well as for the outflow of plasma-spheric material in the inner magnetosphere. The electric field could be obtained from the potential pattern by calculating its gradient, when an inductive component is negligible. Such an assumption seems to be valid when we consider the electric field averaged over a long time interval. The reason why a potential pattern is usually discussed instead of an electric field pattern itself is that it is easy to visualize a potential pattern because contour levels of the potential pattern correspond to the streamline of convection. Historically, *Volland* [1973] and *Stern* [1975] established a semi-empirical analytical model of the electric potential in the equatorial region by combining corotating potential and convection potential based on the

measurement of the location of the plasmopause. A shielding effect by the ionosphere was taken into account for the convection potential. *Maynard and Chen* [1975] and *Gussenhoven et al.* [1981] determined functions of Kp index to scale the size of the convection potential so that it is possible to estimate the electric field at any point once Kp index is given. Although the formula is much simplified, many aspects of particle behaviors can be explained by this model and this model is often used [e.g., *Thomsen et al.*, 2002]. Other empirical potential patterns at the equator were obtained by *McIlwain* [1974, 1986] from particle data at geosynchronous orbits. These models are also expressed with a small number of variables and equations so that the electric field can be easily calculated. At the low and middle latitudes of the ionosphere, *Richmond* [1976] and *Richmond et al.* [1980] determined the electric potential during quiet days. They used data from ground measurements by radars and whistler duct drifts. The potential was expanded into a spherical harmonic function.

[3] It is common to derive potential patterns in the polar regions of the ionosphere. *Heppner* [1972, 1977] gave potential patterns as pictorial forms from probe measurements by OGO 6. Since then, various potential patterns were proposed based on observations by probe instruments and ion drift meters on board spacecraft and by ground facilities such as radars and magnetometers [e.g., *Heelis et al.*, 1982; *Foster*, 1986; *Heppner and Maynard*, 1987; *Rich and Hairston*, 1994; *Papitashvili et al.*, 1994]. Some of these patterns are given as either an analytic form or a table value so that comparisons with other observations are possible. *Weimer* [1995, 1996, 2001] fitted potential patterns by spherical harmonic coefficients, in which it is not necessary to have a bin-averaging process at each grid point. This approach is fairly common in subsequent works [*Ruohoniemi and Greenwald*, 1996; *Papitashvili and Rich*, 2002].

[4] *Fejer and Scherliess* [1997] followed another method to investigate time variation rather than spatial variation dealt with in the above works, although they do not derive potential patterns. They analyzed one component of electric fields during storm time periods from equatorial radar measurements and showed that it is necessary to follow the time history during these active periods in order to construct a good model. *Burke et al.* [1998] also mentioned the dynamic features of the stormtime electric field. Another approach is a real-time calculation of a potential pattern such as the assimilative mapping of ionospheric electro-dynamics (AMIE) [*Richmond and Kamide*, 1988; *Richmond*, 1992]. In this case one modeled electric potential pattern is given as a prior parameter, and then this pattern is adjusted to match various real-time measurements such as ground magnetometers and spacecraft electric field instruments. A similar technique is employed to get a real-time potential pattern during the operation of ground radar measurements [*Ruohoniemi and Baker*, 1998].

[5] In this study, we derive electric potential patterns in the equatorial region of the inner magnetosphere at $L = 4-10$ and at all MLT ranges, using for the first time in situ data (both components of the electric field perpendicular to the magnetic field direction) from Cluster Electron Drift Instrument (EDI) [*Paschmann et al.*, 1997, 2001]. This study is an extension of our previous work, in which average electric field vectors were derived in the same region and were compared with those in previous works [*Matsui et al.*, 2003]. Although many of the previous potential patterns are obtained at the ionospheric level, we derive potential patterns in the equatorial region because of the possibility of direct comparison with the ring current distributions and/or with the images of density profiles of the plasmasphere. Our potential patterns may also be applied to real-time potential calculation schemes as discussed in the above paragraph.

[6] The paper is organized as follows. First, we explain the data set from Cluster EDI in section 2. Then we discuss the dependence of the electric field on the following parameters in order to define a suitable parameterization of the potential patterns in section 3: the Z component of the interplanetary magnetic field (IMF), Kp index, and Dst index. Calculation of potential patterns follows in section 4. In this initial study we develop a method in which an inverse problem is solved to get tables of empirical potential patterns for (1) IMF $B_Z > 0$ and < 0 ; (2) $Kp < 2$, $2 \leq Kp < 4$,

and $4 \leq Kp$; and (3) $F(Dst^*) (\equiv dDst^*/dt + 0.13Dst^*) > 0$ and < 0 , where the effect of the magnetopause current is removed in Dst^* . More refined parameterization will be considered in future model development as the EDI data set expands. The choice of an optimal trade-off parameter is described. We discuss physical implications of the obtained patterns in section 5. Finally, we offer conclusions in section 6.

2. Data Set

[7] In this study we use data from EDI on three spacecraft (SC 1, 2, and 3) of Cluster. Although Cluster consists of four spacecraft, the EDI on SC 4 is not operated. Details of the instrument are described in the work of *Paschmann et al.* [1997, 2001]. The EDI measures the drift motion of electron beams with an energy of 500 eV or 1 keV emitted from guns. The electron motion consists of $E \times B$ drift and slight amounts of gradient B drift. We determine the electric field from the $E \times B$ drift motion. The interval of the data we analyze is ~ 2 years between 18 February 2001 and 16 February 2003 so that the full range of magnetic local time (MLT) is scanned twice. This database is extended from that of the previous study by *Matsui et al.* [2003]. We use data with a time resolution of the ground analysis, 1 s, although there is a data gap from time to time because of lack of return beams. These data are further averaged to 5 min and then mapped to the magnetic equator by using a magnetic field model of *Tsyganenko and Stern* [1996]. At the same time, the effect of the gradient B drift is removed using this model. A typical magnitude of the gradient B drift included in the measured electric field was ~ 0.1 mV/m at most as estimated in the work of *Matsui et al.* [2003]. As solar wind data are input parameters of this magnetic field model, we use data taken from ACE [*Smith et al.*, 1998; *McComas et al.*, 1998]. A propagation delay is taken into account by calculating the X coordinates of the spacecraft position in the geocentric solar ecliptic (GSE) coordinate system from $X_{GSE} = 0$ divided by solar wind speeds.

[8] We use IMF B_Z in the geocentric solar magnetospheric (GSM) coordinate system, Kp index, and Dst index as indicators of geomagnetic activity. Although IMF B_Z is not an activity parameter, geomagnetic activity increases as polarity of IMF B_Z turns from positive to negative. IMF B_Z components are shifted by the time lags as noted in the above paragraph.

3. Dependence of Electric Field on IMF B_Z Component, Kp Index, and Dst Index

[9] In this section we discuss how the electric field is organized by the following parameters in order to construct potential patterns: IMF B_Z component, Kp index, and Dst index. We correlate each parameter with the X and Y components of the electric field with a resolution of 5 min at each spatial bin with a size of $\Delta L = 1 R_E$ and an MLT width of 1 hour. The electric field is calculated in the solar magnetospheric (SM) coordinate system. Figures 1a and 1b show two examples of the comparison between the IMF B_Z component and the Y component of the electric field. IMF B_Z is averaged for 40 min prior to and during each data interval. A bin at $L = 8-9$ and 1800-1900 MLT is chosen in Figure 1a. E_Y increases as IMF B_Z decreases as expected. IMF B_Z and E_Y have a negative correlation with a correla-

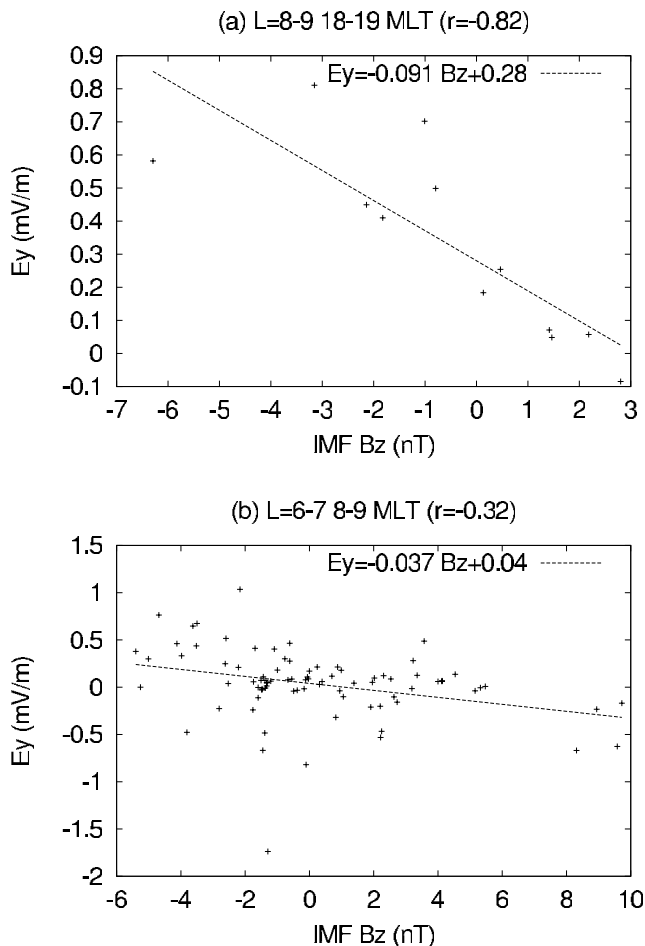


Figure 1. Scatterplots between IMF B_z and E_y from Cluster. E_y is averaged for 5 min, while IMF B_z is averaged for 40 min. The location of Cluster is (a) at $L = 8-9$ and at 1800–1900 MLT and (b) at $L = 6-7$ and at 0800–0900 MLT. The regression line is shown as a dashed line.

tion coefficient of -0.82 . Another bin at $L = 6-7$ and 0800–0900 MLT is chosen in Figure 1b. Although the data points are scattered compared to the previous example in Figure 1a, we can see a negative correlation between IMF B_z and E_y . A correlation coefficient is -0.32 in this case.

[10] We extend the same analysis for other spatial bins with a total number of 144 (six in the radial direction between $L = 4.5-9.5$ and 24 in the azimuthal direction between 0030–2330 MLT). Figure 2a shows a frequency distribution of the number of 5 min data in each spatial bin as a reference. The average number of 5 min data in each bin is 64. Figures 2b and 2c show frequency distributions of correlation coefficients for E_x and E_y , respectively. There are no bins with correlation coefficients ~ 0 because we count only those bins with significant correlations. Here we define a bin with significant correlation as the bin in which the hypothesis that electric fields and IMF B_z are not correlated is rejected with a significant level of 95%. In our statistics it is possible to include multiple points from one orbit in a bin. We deal with points sampled in different times independently because solar wind conditions vary in time. However, data points from multiple spacecraft are

converged to one data point because we set a spatial resolution of a bin size. By comparing these two figures, there are more bins with significant correlations for the E_y component than those for the E_x component presumably because the interplanetary electric field (IEF) affects the magnetospheric convection electric fields. The total numbers of bins with correlations are actually 50 and 83 for E_x and E_y , respectively. There are bins with absolute values of correlation coefficients below 0.5. One reason for these small correlation coefficients is that dependencies are complex and not single variable, perhaps because of previous activity histories. Figures 2d and 2e show frequency distributions of slopes of E_x and E_y to IMF B_z , respectively. In Figure 2e the slopes are mostly negative values with -0.05 ± 0.03 (mV/m)/nT, where we note an average and a standard deviation, respectively. When this value is divided by the solar wind speed, it corresponds to the ratio of the magnetospheric electric field to the IEF, namely the efficiency of the penetration of the IEF into the magnetosphere. If we assume a typical solar wind speed of 450 km/s, the efficiency is estimated as 0.11 ± 0.07 . This value is close to a typical value of the efficiency of 0.075 as can be inferred from *Siscoe and Crooker* [1974]. From this point it is again possible to infer that the effect of the IEF is observed by Cluster. A similar value of the slope is seen for the E_x component (Figure 2d), which indicates that this component is also affected by the IEF, although the correlation is less compared with that of the E_y component.

[11] In the previous paragraphs the IMF B_z component was averaged for 40 min, which was selected as an appropriate interval to calculate averages for IMF B_z as follows. We chose various time intervals between 5 min and 12 hours. Figure 3 shows numbers of spatial bins with significant correlations between each component of electric fields and IMF B_z . The horizontal axis shows intervals to calculate averages for IMF B_z . Peak numbers of spatial bins with correlations are obtained with the averaging interval of $\sim 35-55$ min. Thus we select the averaging interval of 40 min, which is the same as chosen by *Weimer* [1995] and *Matsui et al.* [2003].

[12] As for the Kp index, we calculate the numbers of spatial bins with correlation for E_x and E_y components as 58 and 87, respectively. These numbers are similar to those for the IMF B_z component, as discussed in the above paragraphs. The Kp index is correlated with the electric field as well as the IMF B_z . The number of spatial bins with correlation for E_y is larger than that for E_x , again indicating the effect of the IEF on the magnetosphere.

[13] Next, we consider the correlation between the electric field at Cluster and the Dst index. First, the effect of the magnetopause current is removed from the original Dst index by following the procedure noted in the work of *Burton et al.* [1975]. The corrected index is noted as Dst^* , which is proportional to the total energy of the ring current. Its time derivative shows the growth or decay rate of the energy. When the following quantity $F(Dst^*) \equiv (dDst^*/dt + 0.13Dst^*)$ is defined, it is proportional to the growth rate of the energy, namely the injection rate of the plasma sheet particles. The quantity $0.13Dst^*$ is related to an average decay rate of the ring current energy. *Burton et al.* [1975] determined the value 0.13 hour^{-1} by comparing Dst^* and $dDst^*/dt$ during northward IMF, when injection of fresh

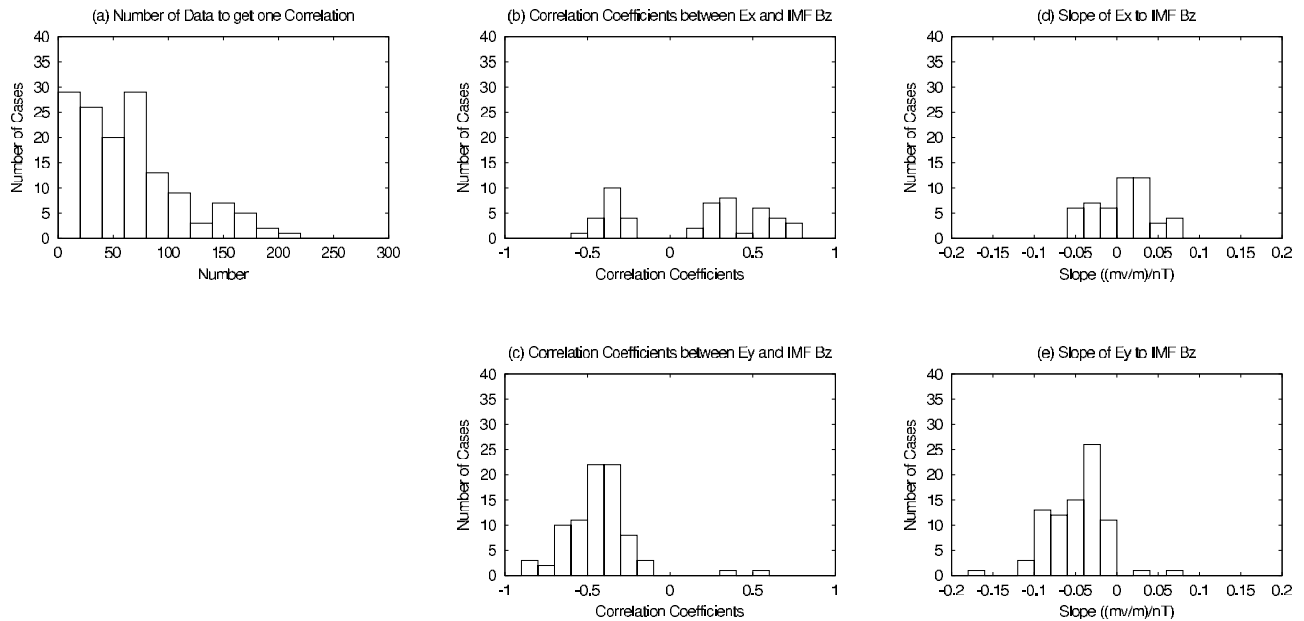


Figure 2. Correlation between two components of the electric field and IMF B_Z . Each panel shows the following quantity: (a) a frequency distribution of the numbers of 5 min data in each spatial bin. (b and c) Frequency distributions of correlation coefficients between each component of electric fields and the IMF B_Z component. (d and e) Frequency distributions of slopes of each component of electric fields to the IMF B_Z component. The unit is in (mV/m)/nT. All except Figure 2a are shown for spatial bins with correlations with a significant level of 95%.

plasma sheet particles is not expected. The numbers of spatial bins with correlation between the electric field and $F(Dst^*)$ are obtained as 44 and 71 for E_X and E_Y , respectively. The slope between E_Y and $F(Dst^*)$ is -0.035 ± 0.026 (mV/m)/(nT/hour). This slope value can be compared with a previous observation by *Burton et al.* [1975] from the following two points. (1) The quantity $F(Dst^*)$ depends on the IEF with a slope of 0.19 (mV/m)/(nT/hour) as suggested by *Burton et al.* [1975]. (2) The IEF is related to the electric field at Cluster, as has been discussed. The efficiency of penetration is 0.11 ± 0.07 . When we combine these two values, the slope of the convection electric field to $F(Dst^*)$ is estimated as -0.021 ± 0.013 (mV/m)/(nT/hour). This value is close to the slope we have obtained above, indicating our work is consistent with *Burton et al.* [1975]. IEF, E_Y at Cluster, and $F(Dst^*)$ are closely related to each other.

[14] As for the spatial distribution of the correlated bins, we have checked it for both components of the electric fields and the following parameters: IMF B_Z , Kp , and $F(Dst^*)$. The number of correlated bins tends to be small at high L and at nighttime, although the actual values are variable for each of the above parameters. The correlation coefficients at the duskside tend to be higher than those at other MLTs.

4. Derivation of Potential Patterns

[15] In the previous section we have inferred that the electric fields in the inner magnetosphere are correlated with the following three parameters: IMF B_Z , Kp , and $F(Dst^*)$. Here we develop a method to estimate potential patterns from these electric fields under the following conditions:

(1) IMF $B_Z > 0$ and < 0 ; (2) $Kp < 2$, $2 \leq Kp < 4$, and $4 \leq Kp$; and (3) $F(Dst^*) > 0$ and < 0 . First, the electric fields are averaged at every grid point at $L = 4.5-9.5$ and 0030–2330 MLT. The data gaps are interpolated up to 3 hour MLT ranges in the azimuthal direction. Then we use a spatial low-pass filter with which the original and neighboring eight points (five points if a bin is located at $L = 4.5$ or 9.5) are averaged. The original points are weighted by a factor of two. This spatial low-pass filter tends to smooth out some small structures and thereby features spatial

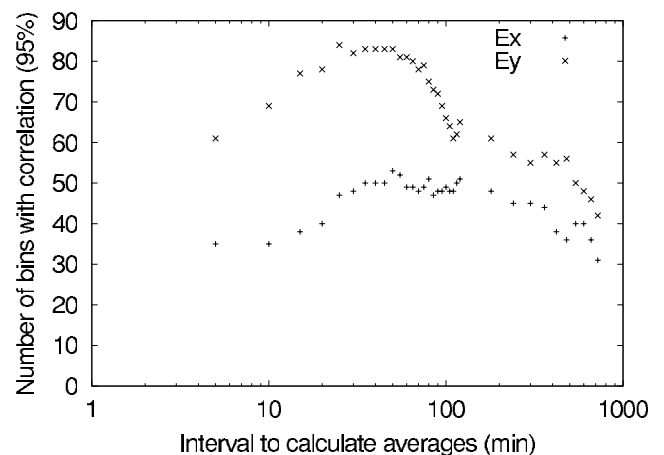


Figure 3. Numbers of spatial bins with correlations between each component of electric fields and IMF B_Z . The intervals to calculate averages of IMF B_Z are between 5 min and 12 hours as shown in the horizontal axis. Correlations are with a significant level of 95%.

structures larger than the scale of smoothing. This spatial filter is similar to that adopted by *Hori et al.* [2000]. The interpolation and smoothing are useful especially for conditions with a small number of data such as $Kp \geq 4$.

[16] Next we solve an inverse problem, which is a technique often employed in data analyses of space physics [e.g., *Richmond and Kamide*, 1988; *Matsui and Hayashi*, 1997; *Korth et al.*, 2002]. The relation between the electric field and the potential is given as follows:

$$e = A\phi, \quad (1)$$

where e is composed of two components of the average electric field vectors perpendicular to the magnetic field at every grid point (288 elements as a whole), A is a matrix as a gradient operator with an additional minus sign, and ϕ is composed of electric potential values at every grid point at $L = 4-10$ and 0000–2300 MLT. The grid points are shifted by $\Delta L = 0.5$ and $\Delta \text{MLT} = 0.5$ hour from those of the electric fields because the electric fields are calculated from variances of the electric potentials. In the above equation, e and A are known parameters, while we would like to get ϕ . The potential is obtained by the following equation:

$$\hat{\phi} = (A^T A + \gamma C^T C)^{-1} A^T e, \quad (2)$$

where $\hat{\phi}$ is composed of estimated values of the potential at each grid point, γ is a trade-off parameter as explained below, and C is a regular matrix and chosen as a Laplacian operator. This matrix requires a spatially smooth result [e.g., *Matsui and Hayashi*, 1997]. As for a boundary condition of the Laplacian operator, the input parameter is assumed to be 0 outside the grid points. It is necessary to choose a suitable value of γ between two opposite situations. When γ is small, equation (2) is close to the original equation (1). However, the result might not be always reliable because the noise included in $\hat{\phi}$ is not reduced. When γ is large, the pattern is excessively smoothed by including a small amount of information from the measured electric fields.

[17] To find a suitable value of γ , one indicator is given as follows:

$$\sigma^2 = \frac{\|A\hat{\phi} - e\|^2}{N_e - N_\phi}, \quad (3)$$

where N_e and N_ϕ are dimensions of vectors e and ϕ , respectively [e.g., *Korth et al.*, 2002]. The relation between γ and σ^2 are plotted in Figure 4 for an example of IMF $B_z > 0$ in a corotating frame. *Korth et al.* [2002] argued that a suitable value of γ can be found where the parameter σ^2 starts to increase. Here we chose the value as indicated by a solid vertical line: $\sigma^2 = 0.99 \min(\sigma^2) + 0.01 \max(\sigma^2)$.

[18] We calculate a potential pattern with equation (2) with the value of γ chosen above ($\gamma = 2.51 \times 10^{-4}$). The electric fields are again derived by equation (1) and are compared with those derived from two different values of γ as plotted with dotted vertical lines in Figure 4 ($\gamma = 2.51 \times 10^{-6}$ and 2.51×10^{-2}). Figure 5 shows radial and azimuthal components of these electric fields with a horizontal axis of MLT. The L value is chosen as 4.5. The following quantities are also plotted: the original electric fields, which are used

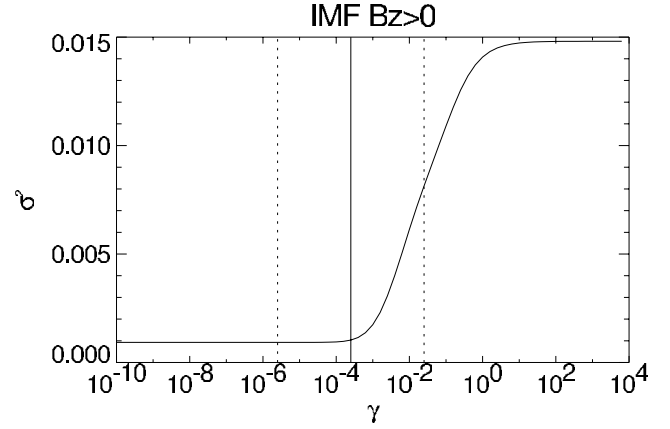


Figure 4. The relation between the trade-off parameter γ and the parameter σ^2 . A suitable value of γ is selected where a value of σ^2 starts to increase as indicated by a vertical line ($\gamma = 2.51 \times 10^{-4}$). Electric fields with γ at the two dotted lines in the figure ($\gamma = 2.51 \times 10^{-6}$ and 2.51×10^{-2}) are calculated in order to compare them with the electric fields with the suitable value of γ .

to solve the inverse problem and are passing through the spatial filter, and the original electric fields without passing through the filter. We can recognize that the electric fields are smoother as values of γ increase. The magnitude of the electric fields with the largest value of γ ($\gamma = 2.51 \times 10^{-2}$) is much smaller than the others, indicating that this value of γ is not realistic. The other two profiles of electric fields ($\gamma = 2.51 \times 10^{-6}$ and 2.51×10^{-4}) are similar to each other for the following two reasons. (1) In Figure 4 the values of σ^2 for $\gamma = 2.51 \times 10^{-6}$ and 2.51×10^{-4} are similar to each other, while σ^2 for $\gamma = 2.51 \times 10^{-2}$ is much larger than the others. It should be noted that the parameter σ^2 defined by equation (3) is proportional to the variance between the original electric fields and those reproduced from the potential pattern. (2) The original electric fields have already been smoothed by the spatial filter so that electric fields with $\gamma = 2.51 \times 10^{-6}$ and 2.51×10^{-4} do not include a significant amount of noise. These two electric fields are similar to the original electric fields, especially for radial components. Azimuthal components have an offset with a maximum size of ~ 0.05 mV/m. It should be noted that an integrated value of azimuthal electric fields for all MLT ranges should be 0 according to Faraday's law, when the electric fields are derived from a potential form. However, this is not always the case for measured electric fields.

[19] Here we consider the accuracy of our measurement. Within a given analysis interval, we determine the electric field from the geometry of the EDI gun/detector unit positions and gun-firing directions for all electron beams that successfully return to their dedicated detector [*Paschmann et al.*, 2001]. Our analysis method, based on triangulation, involves the construction of a penalty function on a two-dimensional (2-D) surface whose minimum ultimately defines the magnitude and direction of the electric field. The penalty surface also yields an error estimate at a chosen confidence level (in this case, 90%), which is based on statistical weighting of the surface using directionally dependent beam-width uncertainties. The error of the esti-

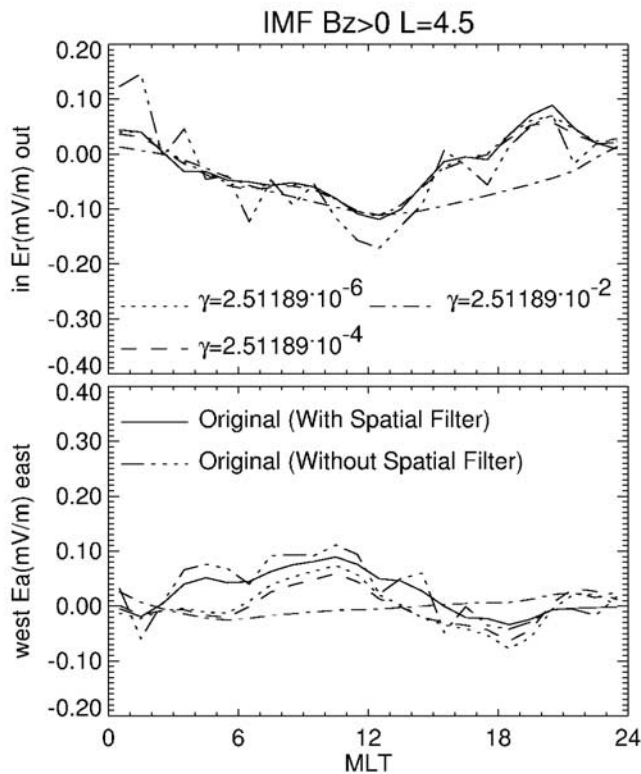


Figure 5. Radial and azimuthal components of the electric fields for IMF $B_z > 0$ at $L = 4.5$. Electric fields are derived from potential patterns with three values of γ : 2.51×10^{-6} , 2.51×10^{-4} , and 2.51×10^{-2} . The following quantities are also plotted: the original electric fields, which are used to obtain the potential patterns and are passing through the spatial filter, and the original electric fields without passing through the filter.

mated electric field therefore is regarded as a random error dependent on gun/detector position and firing angle geometry. The analysis in this paper uses only measurements whose fractional magnitude error is less than 0.3 with a maximum time resolution of 1 s. As we have more than 3000 data points in each spatial bin, the error after averaging decreases to less than 0.6% of the magnitude, which is negligible in our analysis. Another type of error of the measurement is the data gaps due to small numbers of the return beams from the guns. Data gaps tend to exist at the nightside MLT, where larger fluctuation of the electric field exists and the magnitude of the background magnetic field is small [Matsui *et al.*, 2003]. If we assume our measurements on the dayside shown in Figure 5 are correct, it is possible to estimate an average error at the nightside as 0.05 mV/m from the Faraday's law. In the future we plan to introduce data from probe and particle instruments on Cluster in order to supplement our data gaps. A further type of error is the standard error of the mean which is estimated as less than 0.01 mV/m from the data with 5 min resolution. If this small error is a true representation, our potential estimate can be constructed at most with an accuracy of the size of the difference between the measured and modeled electric fields, namely ~ 0.05 mV/m. However, it should be pointed out that our data used to calculate

standard errors are not necessarily independent between each other. In that case, the actual standard error can be larger than expected with a maximum value of 0.2 mV/m which is a standard deviation of the data. Thus it is important to accumulate more independent data from different orbits in the future.

[20] The offset values between the electric fields derived from the potential and the original electric fields are variable depending on MLT which might result from the following reasons. First, the electric fields where there is loss of return beams might depend on MLT. This causes a deviation of the average electric fields from those following the Faraday's law. It is therefore possible that modeled electric fields following Faraday's law and measured electric fields have an offset depending on MLT. Another reason is as follows. When the inverse problem is solved with equation (2), the second derivative of the obtained potential is getting closer to 0 by contribution from the Laplacian matrix C . The electric fields derived from the potential are smoothed as well as the potential, while the original electric fields are not smoothed by the matrix C . The offset values should not necessarily be the same for whole MLT range.

[21] As for the electric field without the spatial filter, there is an offset of ~ 0.05 mV/m to the other profiles for E_r , except $\gamma = 2.51 \times 10^{-2}$ because we have averaged data at $L = 4.5$ and 5.5 through the spatial filter. However, fluctuations in the filtered data are smaller than those without the filter indicating this filter is effective to remove small-scale structures.

5. Potential Patterns and Discussion

[22] In this section we present potential patterns obtained by the above procedure. First, we focus on the patterns for both polarities of IMF B_z . Then we discuss potential patterns organized by K_p index and $F(Dst^*)$. The ASCII values of the potential patterns studied here are attached as supplemental material for comparison with other modeling and/or empirical studies.

[23] Figure 6 shows contour maps of electric potential patterns at $4 < L < 10$ for IMF $B_z > 0$ and IMF $B_z < 0$. Contour intervals are 1 kV and 5 kV for thin and thick lines, respectively. Figures 6a and 6b correspond to the case with IMF $B_z > 0$, while Figures 6c and 6d correspond to the case with IMF $B_z < 0$. The left part of the figure (Figures 6a and 6c) is shown in the corotating frame, while the right part of the figure (Figures 6b and 6d) is shown in the inertial frame. The shaded part in each panel shows the region in which the contour lines are closed around the Earth in the inertial frame. It should be noted that this closed region is located at $L < 4$ in the evening MLT for IMF $B_z < 0$.

[24] One clear feature in the figure is that the potential contours in the corotating frame for IMF $B_z < 0$ (Figure 6c) are denser than those for IMF $B_z > 0$ (Figure 6a) as expected. Such a signature is characterized by a potential difference as defined by the difference between maximum and minimum potential values in the examined spatial area. These values are estimated as 8.5 kV and 23.1 kV for IMF $B_z > 0$ and IMF $B_z < 0$, respectively. We can compare these values with those estimated from the Weimer [2001] model in the same L range ($4 < L < 10$). The potential difference from the Weimer [2001] model is estimated by introducing

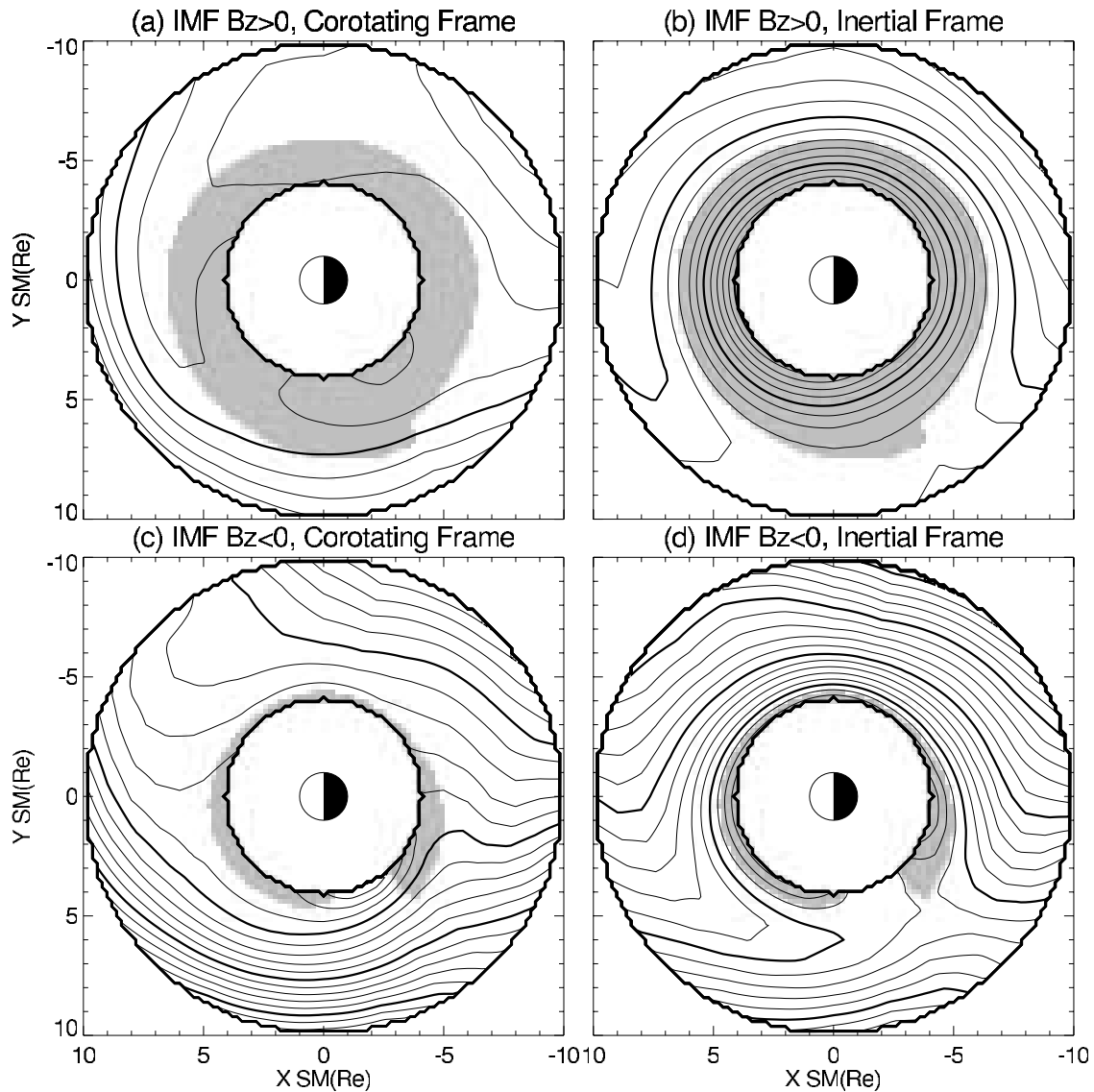


Figure 6. Contour maps of electric potential patterns at $4 < L < 10$ for (a and b) IMF $B_Z > 0$ and for (c and d) IMF $B_Z < 0$. The corotating frame is chosen for Figures 6a and 6c, while the inertial frame is chosen for Figures 6b and 6d. Contour intervals are 1 kV and 5 kV for thin and thick lines, respectively. The shaded area belongs to the closed region, in which the plasmas corotate with the Earth.

average values of the following solar wind quantities from our observations: the strength of the IMF in the Y - Z plane, number density, and velocity. The distributions of clock angles are calculated with a bin width of 45° . The average tilt angles are also introduced from our observations for each MLT bin with a width of 1 hour. The potential difference from the *Weimer* [2001] model is obtained as 16.5 kV (30.8 kV) for IMF $B_Z > 0$ (IMF $B_Z < 0$). These values of the potential difference from Cluster and the *Weimer* [2001] model are summarized in Table 1. It is common for both Cluster observations and the *Weimer* [2001] model that the potential difference for IMF $B_Z < 0$ is larger than that for IMF $B_Z > 0$. Another point is that the potential difference from Cluster is smaller than the potential difference from the *Weimer* [2001] model. One reason for the small value for Cluster is that we have smoothed the electric field to obtain potential patterns. The modeled electric field has $\sim 90\%$ the average amplitude of the

original electric field after passing through the spatial filter and $\sim 73\%$ the average amplitude of the original electric field without the filter.

[25] Another result indicated in Figure 6 is the rotation of the direction of the convection electric fields from the duskward direction at the dayside. The contour lines originating from the nightside pass through the eveningside and lead to the dayside in the corotating frame. If the electric field is duskward, these contours elongate to 1200 MLT. However, the actual destination is rotated from 1200 MLT

Table 1. Potential Difference at $4 < L < 10$ Estimated From Cluster Observations and the *Weimer* [2001] Model

	Cluster	<i>Weimer</i> [2001]
IMF northward, kV	8.5	16.5
IMF southward, kV	23.1	30.8

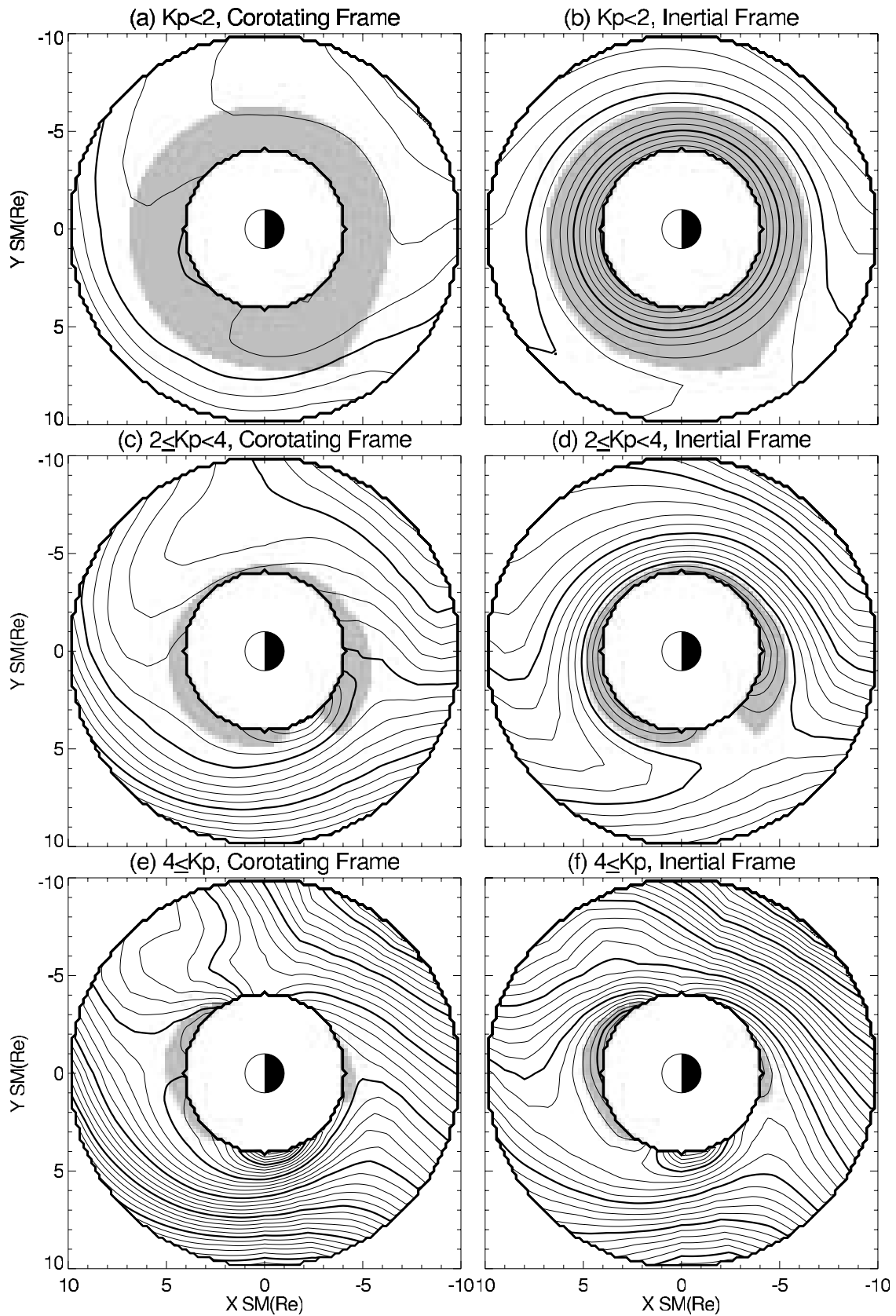


Figure 7. Contour maps of electric potential patterns at $4 < L < 10$ for (a and b) $K_p < 2$, (c and d) $2 \leq K_p < 4$, and (e and f) $4 \leq K_p$. The corotating frame is chosen for Figures 7a, 7c, and 7e, while the inertial frame is chosen for Figures 7b, 7d, and 7f. Contour intervals are 1 kV and 5 kV for thin and thick lines, respectively. The shaded area belongs to the closed region, in which the plasmas corotate with the Earth.

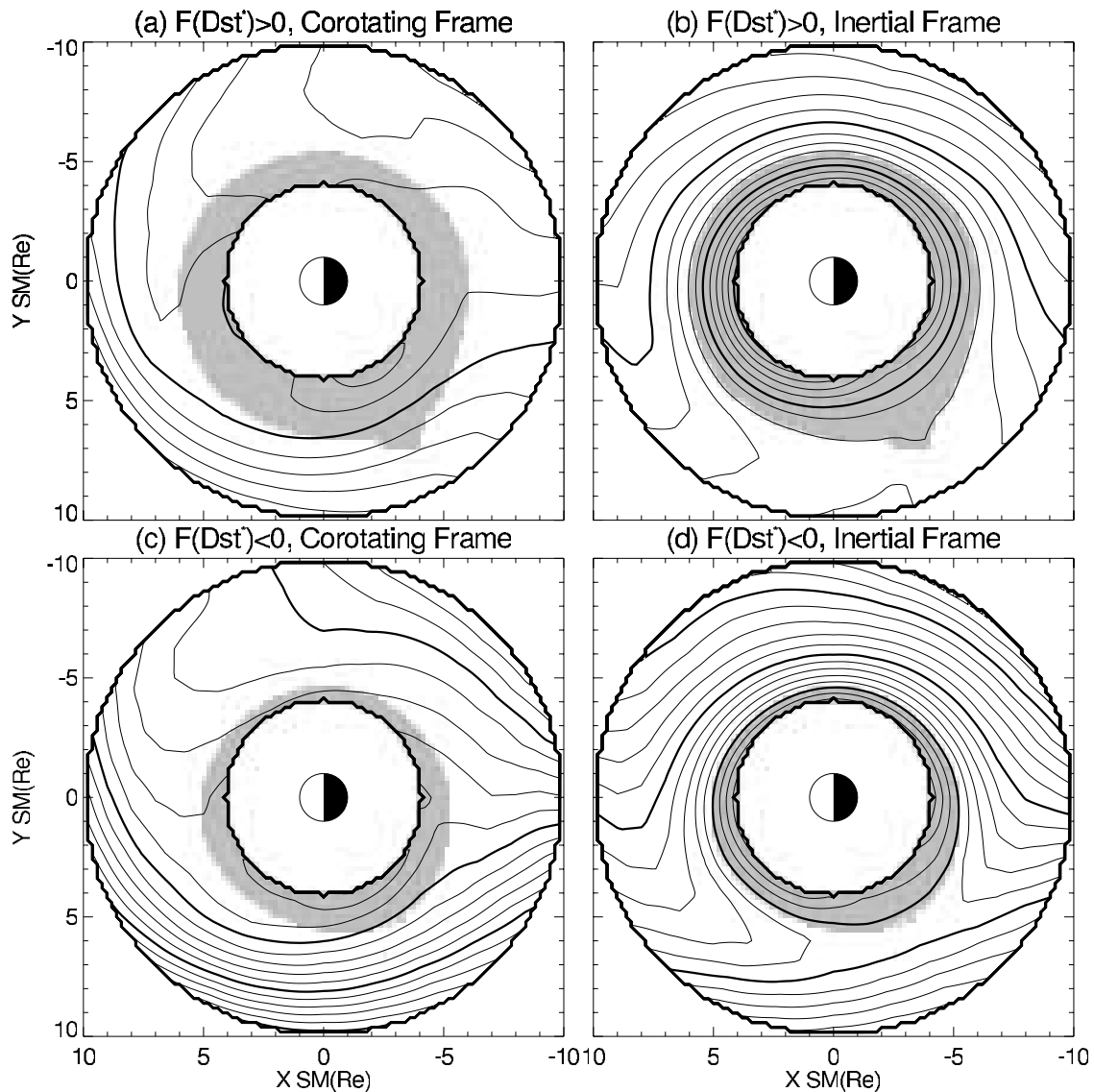


Figure 8. Contour maps of electric potential patterns at $4 < L < 10$ for (a and b) $F(Dst^*) > 0$ and for (c and d) $F(Dst^*) < 0$. The corotating frame is chosen for Figures 8a and 8c, while the inertial frame is chosen for Figures 8b and 8d. Contour intervals are 1 kV and 5 kV for thin and thick lines, respectively. The shaded area belongs to the closed region, in which the plasmas corotate with the Earth.

to ~ 0900 MLT for IMF $B_Z > 0$ and ~ 1100 MLT for IMF $B_Z < 0$ (Figures 6a and 6c). This rotation of the direction of the convection electric field from the duskward direction at the dayside might result from the gradient of the ionospheric conductivity as indicated by *Vasyliunas* [1970]. It should be also noted that the rotation of the direction is dependent on the polarity of IMF B_Z . As the IMF B_Z turns southward, the direction of the convection electric fields at the dayside rotates eastward. This point is qualitatively consistent with *Jordanova et al.* [1998], although they discussed rotation for an event with a higher geomagnetic activity, namely the main phase of a magnetic storm.

[26] A further signature in Figures 6a and 6c is the dawn-dusk asymmetry of the magnitude of the electric fields. One measure for the asymmetry is the variability between the potential difference at 0600 MLT and that at 1800 MLT. The potential difference between $L = 4$ and 10 at 0600 MLT is

estimated as -0.2 kV (6.8 kV), while that at 1800 MLT is estimated as 4.5 kV (15.9 kV) for IMF $B_Z > 0$ (IMF $B_Z < 0$). The potential differences at the duskside are much larger than those at the dawnside for both IMF B_Z polarities. This point is consistent with our previous statistics [*Matsui et al.*, 2003].

[27] We now discuss the potential patterns sorted by Kp index (Figure 7). Patterns are shown for $Kp < 2$ (Figures 7a and 7b), $2 \leq Kp < 4$ (Figures 7c and 7d), and $4 \leq Kp$ (Figures 7e and 7f). The corotating frame is chosen for Figures 7a, 7c, and 7e, while the inertial frame is chosen for Figures 7b, 7d, and 7f. Contour intervals are 1 kV and 5 kV for thin and thick lines, respectively, which is the same as Figure 6. The shaded area indicates the region in which contour lines are closed around the Earth.

[28] We consider the size of the LCE by referring to Figure 7. The LCE corresponds to an approximate location

of the plasmopause, although it is only true when the activity is constant. The LCE with $Kp < 2$ has a typical plasmopause tear-drop shape (Figure 7b). The LCE extends to $L \sim 8$ at 2000 MLT, while it is at $L \sim 6$ in the morningside. The LCE shrinks with $2 \leq Kp < 4$ (Figure 7d). It is located at $L \sim 6$ at 2100 MLT, while it is at $L \sim 4.5$ in the morningside. The LCE shrinks further for $4 \leq Kp$ (Figure 7f). The LCE is at most at $L \sim 5$.

[29] Finally, we focus on Figure 8, in which the potential patterns for $F(Dst^*) > 0$ and < 0 are shown. The format of this figure is the same as Figures 6 and 7. General features such as denser contour lines for more active cases and the dawn-dusk asymmetry are common to the patterns sorted by IMF B_z and Kp .

6. Conclusions

[30] We have derived electric potential patterns in the equatorial magnetosphere at $4 < L < 10$, using 2 years of data from Cluster EDI. First, relations between the electric field and the following three parameters were investigated in order to organize the data: IMF B_z , Kp index, and Dst index. We inferred the influence of the IEF on the electric field at Cluster. The Kp index was correlated with the average electric field. We also correlated the electric field with the quantity $F(Dst^*)$ representing the injection rate of the plasma sheet particles. Next, we developed a method to derive potential patterns solving an inverse problem and introducing a trade-off parameter. The electric fields derived from the potential patterns and the original electric fields before solving the inverse problem were compared in order to evaluate the methodology adopted. In this initial study we considered the following parameterization for the potential patterns: (1) IMF $B_z > 0$ and < 0 ; (2) $Kp < 2$, $2 \leq Kp < 4$, and $4 \leq Kp$; and (3) $F(Dst^*) > 0$ and < 0 . More refined parameterization will be considered in future as the EDI data set increases. The resulting potential patterns are attached as supplemental material. We reached the following conclusions by examining the potential patterns derived. (1) The potential contours for IMF $B_z < 0$ are denser than those for IMF $B_z > 0$ in the corotating frame. (2) The direction of the convection electric field is rotated from the dawn-dusk direction at the dayside. (3) A substantial dawn-dusk asymmetry of the electric field is seen in the potential contours with more intense electric field near the duskside. (4) The size of the LCE shrinks as the Kp index increases.

[31] **Acknowledgments.** We thank the many members of the EDI team for innumerable contributions to the design, development, and operation of EDI, and to the ground processing of the data. We thank P. A. Puhl-Quinn for EDI data processing and many helpful discussions. We are grateful to A. Balogh and the Cluster FGM team for providing the magnetic field data used by EDI on board and in ground processing, and to N. Cornilleau-Wehrin and the STAFF team for providing the onboard STAFF data. We acknowledge N. F. Ness and D. J. McComas for the ACE MAG and SWEPAM data provided through CDA website, respectively. This work was supported by NASA through grant NAG5-9960 and NSF through grant ATM0309585.

[32] Arthur Richmond thanks the reviewers for their assistance in evaluating this paper.

References

- Burke, W. J., N. C. Maynard, M. P. Hagan, R. A. Wolf, G. R. Wilson, L. C. Gentile, M. S. Gussenhoven, C. Y. Huang, T. W. Garner, and F. J. Rich (1998), Electrodynamics of the inner magnetosphere observed in the dusk

- sector by CRRES and DMSP during the magnetic storm of June 4–6, 1991, *J. Geophys. Res.*, *103*, 29,399–29,418.
- Burton, R. K., R. L. McPherron, and C. T. Russell (1975), An empirical relationship between interplanetary conditions and Dst , *J. Geophys. Res.*, *80*, 4204–4214.
- Fejer, B. G., and L. Scherliess (1997), Empirical models of storm time equatorial zonal electric fields, *J. Geophys. Res.*, *102*, 24,047–24,056.
- Foster, J. C. (1986), Ionospheric convection associated with discrete levels of particle precipitation, *Geophys. Res. Lett.*, *13*, 656–659.
- Gussenhoven, M. S., D. A. Hardy, and W. J. Burke (1981), DMSP/F2 electron observations of equatorward auroral boundaries and their relationship to magnetospheric electric fields, *J. Geophys. Res.*, *86*, 768–778.
- Heelis, R. A., J. K. Lowell, and R. W. Spiro (1982), A model of the high-latitude ionospheric convection pattern, *J. Geophys. Res.*, *87*, 6339–6345.
- Heppner, J. P. (1972), Polar-cap electric field distributions related to the interplanetary magnetic field direction, *J. Geophys. Res.*, *77*, 4877–4887.
- Heppner, J. P. (1977), Empirical models of high-latitude electric fields, *J. Geophys. Res.*, *82*, 1115–1125.
- Heppner, J. P., and N. C. Maynard (1987), Empirical high-latitude electric field models, *J. Geophys. Res.*, *92*, 4467–4489.
- Hori, T., K. Maezawa, Y. Saito, and T. Mukai (2000), Average profile of ion flow and convection electric field in the near-earth plasma sheet, *Geophys. Res. Lett.*, *27*, 1623–1626.
- Jordanova, V. K., C. J. Farrugia, L. Janoo, J. M. Quinn, R. B. Torbert, K. W. Ogilvie, R. P. Lepping, J. T. Steinberg, D. J. McComas, and R. D. Belian (1998), October 1995 magnetic cloud and accompanying storm activity: Ring current evolution, *J. Geophys. Res.*, *103*, 79–92.
- Korh, H., M. F. Thomsen, K.-H. Glassmeier, and W. S. Phillips (2002), Particle tomography of the inner magnetosphere, *J. Geophys. Res.*, *107*(A9), 1229, doi:10.1029/2001JA000147.
- Matsui, H., and K. Hayashi (1997), Positioning of auroral arcs in all-sky TV images as an inverse problem, *Phys. Chem. Earth*, *22*, 723–728.
- Matsui, H., J. M. Quinn, R. B. Torbert, V. K. Jordanova, W. Baumjohann, P. A. Puhl-Quinn, and G. Paschmann (2003), Electric field measurements in the inner magnetosphere by Cluster EDI, *J. Geophys. Res.*, *108*(A9), 1352, doi:10.1029/2003JA000913.
- Maynard, N. C., and A. J. Chen (1975), Isolated cold plasma regions: Observations and their relation to possible production mechanisms, *J. Geophys. Res.*, *80*, 1009–1013.
- McComas, D. J., S. J. Bame, P. Barker, W. C. Feldman, J. L. Phillips, P. Riley, and J. W. Griffiee (1998), Solar wind electron proton alpha monitor (SWEPAM) for the advanced composition explorer, *Space Sci. Rev.*, *86*, 563–612.
- Mcllwain, C. E. (1974), Substorm injection boundaries, in *Magnetospheric Physics*, edited by B. M. McCormac, pp. 143–154, D. Reidel, Norwell, Mass.
- Mcllwain, C. E. (1986), A Kp dependent equatorial electric field model, *Adv. Space Res.*, *6*(3), 187–197.
- Papitashvili, V. O., and F. J. Rich (2002), High-latitude ionospheric convection models derived from Defense Meteorological Satellite Program ion drift observations and parameterized by the interplanetary magnetic field strength and direction, *J. Geophys. Res.*, *107*(A8), 1198, doi:10.1029/2001JA000264.
- Papitashvili, V. O., B. A. Belov, D. S. Faermark, Y. I. Feldstein, S. A. Golyshev, L. I. Gromova, and A. E. Levitin (1994), Electric potential patterns in the northern and southern polar regions parameterized by the interplanetary magnetic field, *J. Geophys. Res.*, *99*, 13,251–13,262.
- Paschmann, G., et al. (1997), The Electron Drift Instrument for Cluster, *Space Sci. Rev.*, *79*, 233–269.
- Paschmann, G., et al. (2001), The Electron Drift Instrument on Cluster: Overview of first results, *Ann. Geophys.*, *19*, 1273–1288.
- Rich, F. J., and M. Hairston (1994), Large-scale convection patterns observed by DMSP, *J. Geophys. Res.*, *99*, 3827–3844.
- Richmond, A. D. (1976), Electric field in the ionosphere and plasmasphere on quiet days, *J. Geophys. Res.*, *81*, 1447–1450.
- Richmond, A. D. (1992), Assimilative mapping of ionospheric electro-dynamics, *Adv. Space Res.*, *12*(6), 59–68.
- Richmond, A. D., and Y. Kamide (1988), Mapping electrodynamic features of the high-latitude ionosphere from localized observations: Technique, *J. Geophys. Res.*, *93*, 5741–5759.
- Richmond, A. D., et al. (1980), An empirical model of quiet-day ionospheric electric fields at middle and low latitudes, *J. Geophys. Res.*, *85*, 4658–4664.
- Ruohoniemi, J. M., and K. B. Baker (1998), Large-scale imaging of high-latitude convection with Super Dual Auroral Radar Network HF radar observations, *J. Geophys. Res.*, *103*, 20,797–20,811.

- Ruohoniemi, J. M., and R. A. Greenwald (1996), Statistical patterns of high-latitude convection obtained from Goose Bay HF radar observations, *J. Geophys. Res.*, *101*, 21,743–21,763.
- Siscoe, G., and N. Crooker (1974), A theoretical relation between Dst and the solar wind merging electric field, *Geophys. Res. Lett.*, *1*, 17–19.
- Smith, C. W., J. L'Heureux, N. F. Ness, M. H. Acuña, L. F. Burlaga, and J. Scheifele (1998), The ACE magnetic fields experiment, *Space Sci. Rev.*, *86*, 613–632.
- Stern, D. P. (1975), The motion of a proton in the equatorial magnetosphere, *J. Geophys. Res.*, *80*, 595–599.
- Thomsen, M. F., H. Korth, and R. C. Elphic (2002), Upper cutoff energy of the electron plasma sheet as a measure of magnetospheric convection strength, *J. Geophys. Res.*, *107*(A10), 1331, doi:10.1029/2001JA000148.
- Tsyganenko, N. A., and D. P. Stern (1996), Modeling the global magnetic field of the large-scale Birkeland current systems, *J. Geophys. Res.*, *101*, 27,187–27,198.
- Vasyliunas, V. M. (1970), Mathematical models of magnetospheric convection and its coupling to the ionosphere, in *Particles and Fields in the Magnetosphere*, edited by B. M. McCormac, pp. 60–71, D. Reidel, Norwell, Mass.
- Volland, H. (1973), A semiempirical model of large-scale magnetospheric electric fields, *J. Geophys. Res.*, *78*, 171–180.
- Weimer, D. R. (1995), Models of high-latitude electric potentials derived with a least error fit of spherical harmonic coefficients, *J. Geophys. Res.*, *100*, 19,595–19,607.
- Weimer, D. R. (1996), A flexible IMF dependent model of high-latitude electric potentials having “space weather” applications, *Geophys. Res. Lett.*, *23*, 2549–2552.
- Weimer, D. R. (2001), An improved model of ionospheric electric potentials including substorm perturbations and applications to the Geospace Environment Modeling November 24, 1996, event, *J. Geophys. Res.*, *106*, 407–416.
-
- V. K. Jordanova, H. Matsui, J. M. Quinn, and R. B. Torbert, Space Science Center, University of New Hampshire, Morse Hall, Durham, NH 03824, USA. (vania.jordanova@unh.edu; hiroshi.matsui@unh.edu; jack.quinn@unh.edu; roy.torbert@unh.edu)
- G. Paschmann, Max-Planck-Institut für extraterrestrische Physik, P.O. Box 1603, D-85740 Garching, Germany. (goetz.paschmann@mpe.mpg.de)